



Showcasing research from Professor Ah-Hyung Alissa Park's laboratory, Dept. of Earth and Environmental Engineering, Columbia University, New York City, United States of America.

Hybrid thermo-electrochemical conversion of plastic wastes commingled with marine biomass to value-added products using renewable energy

Marine plastic wastes commingled with biomass are one of the biggest environmental challenges in the oceans and coastal areas. These mixed marine wastes have no economic value and are harmful to ocean ecosystems. Its presence also promotes the formation of microplastics which degrade and enter food supply chains. In this work, we have developed a novel hybrid thermo-electrochemical conversion technology that upgrades plastic wastes mixed with marine biomass to carbon-free bio-H₂, purified polymeric materials, and carbon nanotubes, effectively turning waste into value-added products and energy carriers.

As featured in:



See Ah-Hyung Alissa Park *et al.*, *Energy Environ. Sci.*, 2023, **16**, 5805.

Cite this: *Energy Environ. Sci.*,
2023, 16, 5805

Hybrid thermo-electrochemical conversion of plastic wastes commingled with marine biomass to value-added products using renewable energy†

Jonah M. Williams,^a Michael P. Nitzsche,^b Lev Bromberg,^b Zifeng Qu,^c
Aaron J. Moment,^c T. Alan Hatton^b and Ah-Hyung Alissa Park^{*,acd}

Surface plastics and microplastics commingled with biomass are emerging pollutants in the marine environment. With the projected demand for plastics sharply increasing, innovative methods of abating these end-of-life (EOL) marine plastic wastes are necessary. Thermochemical methods to convert plastics and biomass are potential candidates for this task, although anthropogenic CO₂ emissions are often inevitable. Alkaline thermal treatment (ATT) is a promising thermochemical conversion technology, running at moderate conditions (<600 °C, 1 atm) and fixing carbon in the form of stable carbonate salts (e.g., Li₂CO₃ and K₂CO₃). Carbonate salts can be electrochemically converted to high purity carbon nanotubes (CNTs) using renewable energy (e.g., offshore wind energy). Herein, the integration of these two technologies is studied in the context of a novel tandem thermo-electrochemical (elecATT) process to treat and upcycle marine wastes. This study shows that our novel elecATT of polyethylene and salty brown seaweed performed at 500–600 °C can produce hydrogen at high purity (85%), and these reactions can be enhanced by the presence of both heterogeneous *in situ* and *ex situ* γ-zeolite and Ni/ZrO₂ catalysts. The majority of carbon from seaweed and plastics was converted to carbonate ions in a molten electrolyte composed of Li₂CO₃/K₂CO₃/LiOH and converted to carbon nanotubes *via* electrosplitting of carbonate ions with near 100% Coulombic efficiency. Carbon analysis was performed to analyze the fate of carbon throughout the elecATT reactions, and to evaluate the recyclability of LiOH/KOH electrolytes for the ATT reaction. Overall, this study presents an innovative method for the treatment and upgrading of marine plastic pollutants by producing high purity H₂ and purified polymer intermediates for upcycling, and capturing carbon *via* a molten salt which can then be electrochemically converted to produce high-value CNTs using renewable energy.

Received 27th July 2023,
Accepted 23rd October 2023

DOI: 10.1039/d3ee02461j

rsc.li/ees

Broader context

End-of-life (EOL) mismanaged plastic waste streams entering the marine environment are a ubiquitous, large-scale problem requiring innovative solutions. With plastic production projected to increase in the next quarter century, especially in industrializing regions with poor waste management infrastructures, marine surface plastic pollution will continue to increase. These wastes are often infeasible to trace their places of origin to discourage emission. Marine plastic wastes cannot be recycled directly because of their heterogeneity in compositions and commingling with wet and salty marine biomass. Therefore, there are often no economic incentives to collect and treat these wastes. However, if left untreated the issue of marine plastic pollution could cause catastrophic consequences for the global marine biome and will directly impact human life through the collapse of fishing ecosystems. Herein, we propose and demonstrate a method to treat marine plastic wastes commingled with biomass *via* a novel thermo-electrochemical conversion technology with molten salts. This process produces high-purity hydrogen and carbon nanotubes (CNTs) from the wastes, while fixing and sequestering carbon. This technology can be installed offshore utilizing solar heat and wind electricity. This novel approach adds economic incentive to facilitate clean-up efforts *via* the creation of high-value products while also affording a volumetric reduction of wastes to be transported to the shore.

^a Department of Earth and Environmental Engineering, Columbia University, New York, New York, 10027, USA. E-mail: ap2622@columbia.edu^b Department of Chemical Engineering, Massachusetts Institute of Technology, Cambridge, Massachusetts, 02138, USA^c Department of Chemical Engineering, Columbia University, New York, New York, 10027, USA^d Lenfest Center for Sustainable Energy, Columbia University, New York, New York, 10027, USA† Electronic supplementary information (ESI) available. See DOI: <https://doi.org/10.1039/d3ee02461j>

Introduction

Plastic products are widely used in contemporary human life, ranging from plastic bags and food containers to cloth fragments, tires, and shipping containers. Through convenience, low cost and high durability, plastics have become extremely omnipresent.^{1,2} Research suggests that human-manufactured plastics have touched almost all places on Earth.^{3,4} Since the end of World War II, there has been an exponential growth in plastic production. Current forecasts predict that the production of plastics will only increase due to the urbanization and industrialization of many developing economies. This is reflected in demand by plastic manufacturers for commodity chemicals such as ethylene, propylene, and styrene, especially in countries such as China and Korea.⁵ Additionally, refining industries are shifting away from transportation fuels and moving towards producing naphtha and upgrading residues which can be used as feedstocks for naphtha reformers (aromatics) and steam crackers (ethylene, propylene); such processes are already being commercialized, such as Crude-Oil-to-Chemicals (COTC, Aramco/SABIC).^{5,6}

In an effort to standardize the organization of plastics and facilitate recycling efforts to curb single-use plastic pollution, the U.S. Society of the Plastics Industry introduced the Resin Identification Code (RIC).⁷ These codes correspond to the eight most common plastics, including polyethylene terephthalate (PETE), high-density polyethylene (HDPE), polyvinyl chloride (PVC), low-density polyethylene (LDPE), polypropylene (PP), polystyrene (PS), and others (which includes acrylics, nylons, polycarbonates, *etc.*), as showcased in Fig. 1, which also shows their share of the overall production landscape. Notably, LDPE and PP are the dominant plastics.⁸ The large percentage of LDPE and PP, produced over the period of 2002 to 2014 at 20% and 21%, respectively, is attributed to their significant presence as single-use packaging materials. This is further corroborated by the fact that the largest use of plastic by industry is the packaging market, at about 45%.⁸ Unfortunately, most of the plastic that is produced will never be recycled as it exits the supply chain, destined to end in a landfill or as pollution. Such single-use plastics are both some of the most useful and affordable materials, but are extremely dangerous in terms of their longevity and low degradation potential.³

Mismanaged plastic waste poses a threat to marine environments

The annual global polymer resin and fiber production has increased from around 2 million metric tonnes in 1950 to 381 million metric tonnes in 2015.⁸ The sheer amount of plastic mass produced has led to a number of environmental concerns across the globe, especially in regards to ecosystem degradation. Plastics are highly desired materials due to their resistivity and durability; however, this is also a bane as their hydrocarbon nature results in natural degradation times of hundreds or thousands of years.⁹ A large percentage of plastics in the global supply chain are mismanaged, meaning they are either littered as refuse or inadequately disposed.¹⁰ More than



Fig. 1 The eight major plastic polymer types, their corresponding resin identification code (RIC), and their relative share of the global industrial plastic production landscape. Data adapted from Geyer *et al.*⁸

8 million tonnes of plastic end up in the marine environment each year, with more than 10 000 tonnes becoming surface water plastics (Fig. 2).^{10,11}

This surface and subsurface plastic is quite harmful to various marine trophic levels, and accumulates in large quantities in certain ocean areas due to currents (*e.g.*, the Pacific Ocean Gyres: colloquially “The Great Pacific Garbage Patch”).^{4,12,13} Nets, bags, and storage containers can entangle and trap larger sea creatures. Colorful items are often mistaken for food by birds and fish. Smaller pieces, oftentimes microscopic (*e.g.*, “microplastics”), are a result of the harsh ultraviolet (UV) radiation and highly saline water, which can lead to oxidative degradation, decreasing plastic size over time.¹⁴ These microplastics can be consumed and assimilated by organisms such as plankton and krill, which can then undergo biomagnification up the food chain. Microplastics are a concerning issue not only for natural marine ecosystems but also for human activities in marine environments; they could physically harm humans and collapse fishing economies.¹⁵

The proliferation of mismanaged plastic wastes is projected to grow significantly in the next 30 years, fueled by industrialization and population growth.¹⁰ According to extrapolated projections based on the methodologies established by Jambeck *et al.*, it is theorized that most major coastal countries could produce on the order of 500 000 tonnes of mismanaged plastic waste per year by 2040 (Fig. S1, ESI†).¹⁰ Efforts to mitigate marine plastic pollution are currently lacking. Curbing production and managing coastal waste streams would aid in reducing the flow of wastes to the ocean.¹⁶ However, addressing the vast amounts of marine waste already present in the ocean

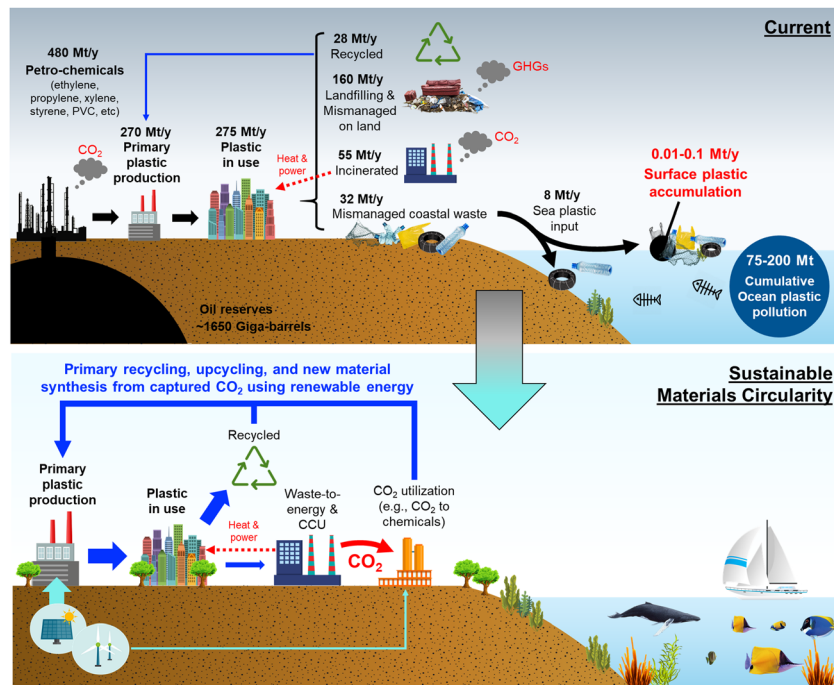


Fig. 2 Global plastic production, current methods of disposal, and accumulation pathways of coastal wastes in today's world with a future vision for sustainable material circularity combined with carbon capture and utilization (CCU). A large percentage of coastal waste ends up as mismanged coastal waste which can eventually wash into the ocean. Certain data sourced from Ritche and Roser (2015).¹⁴

will require removal and clean-up technologies. Clearly the scale and magnitude of this issue, potential continued catastrophic ecosystem damage, and impact on human global food supply chains warrants increased attention and action.

Contamination and commingling of plastic wastes with marine biomass

The deposition of plastic at various ocean strata is a function of plastic density, buoyancy, and the changing water density, which is a result of salinity fluctuations. In regards to surface plastics, the largest fractions are composed of LDPE, PS, and PP fishing gear, plastic bottles, and containers due to their relative densities which are less than that of seawater (Fig. S2, ESI†).^{17,18} However, there may be additional types of plastic present on the surface due to the entanglement and commingling of marine species (*e.g.*, biomass) with these waste plastics. It is theorized that this can modulate their buoyancy, in some cases causing a greater fraction to precipitate on the surface. Agglomeration of marine plastics can also be facilitated by biomass commingling. Coupled with marine currents, this can lead to the creation of massive “patches” of plastic wastes.¹² Commingling of marine biomass and plastics happens naturally as the surface plastic provides a medium for tethering and growth. The types of biomass can range from microscopic algal biofilms to large swaths of kelp mingled amongst the plastic. These commingled plastic and biomass deposits are not easily managed due to the harsh conditions of the ocean environment. The presence of high salt concentrations and a variety of contaminants make it infeasible to recover and recycle the plastics in these mixes. Thus, the collected wastes need to be

either landfilled or thermochemically processed, conventionally *via* incineration.

Energetically, the marine plastic and biomass flocs could be promising feedstocks for thermochemical conversion pathways due to their calorific values. The heating value of plastics can vary significantly based on their composition; PVC has an average low heating value (LHV) of 17 MJ kg⁻¹ whereas PE has one of 40 MJ kg⁻¹.¹⁹ Brown seaweeds, due to their high water and heteroatom content have a lower carbon content of about 15–40% depending on the species with a predicted LHV of about 16 MJ kg⁻¹.²⁰ Previous studies have elucidated the primary sugar makeup of these brown seaweeds to be 10–40 wt% alginates (C₆H₈O₆), 2–34 wt% laminarin (C₆H₁₀O₅), 5–25 wt% mannitol (C₆H₁₄O₆), and 5–20 wt% fucoidan (C₇H₁₄O₇S).^{21,22} Due to the high carbon content of marine plastic wastes, they could be ideal candidates for advanced thermochemical conversion pathways whereas they would ordinarily be landfilled or left in the environment.

Novel thermochemical conversion pathway of wet and salty marine biomass

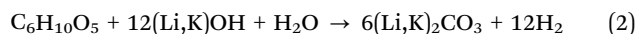
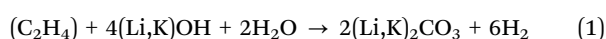
For the thermochemical conversion of commingled marine plastic wastes and biomasses, conventional waste-to-energy (WtE) technologies are not ideal since the feedstock needs to be dried prior to combustion and will lead to large CO₂ emissions unless a carbon capture process is integrated.²³ A few studies have reported on the thermochemical gasification of dried seaweeds and algae, which showed rapid kinetics and the ability to produce synthesis gas rich in H₂/CO which can be used as a fuel itself or for commodity downstream chemicals

(*e.g.*, Fischer–Tropsch drop-in fuels).^{22,24,25} However, the need for dry feedstock is a challenge of these thermal conversion methods due to the high energy intensity of drying and high moisture content of marine seaweeds (>80%). Hydrothermal liquefaction (HTL) of algal biomass can produce bio-crude from a wide variety of oleaginous marine biomasses at moderate temperature (250–400 °C) and elevated pressures (5–20 MPa).²⁶ The robustness of HTL comes from its ability to process algae with water content as high as 92% wt%, which saves energy on pretreatment drying.²⁶ However, the pressure requirement and production of bio-crude might not be advantageous in situations where direct conversion to gaseous products is desired.

Plastic gasification presents its own set of challenges, usually requiring moderate pressures (2–4 MPa) and temperatures (>800 °C) to achieve any appreciable hydrogen production.²⁷ The formation of waxes as well as primary and tertiary tars also occurs due to the viscosity and olefinic/aromatic nature of the plastic feedstocks.²⁷ This can lead to issues with low conversion rates, reactor fouling, and downstream equipment failure.

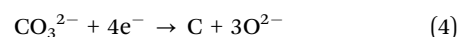
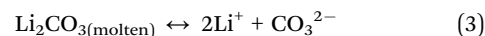
Supercritical water gasification has been studied in the context of both wet biomass and plastics and presents advantages in terms of conversion, hydrogen yield, and reduction of tar, wax, and coke formation.^{27–29} However, high energy consumption, salt scaling, and special reactor metallurgies due to pressure can lead to challenging investment costs.²⁷ Sorption-enhanced gasification methods, utilizing an active gasifier bed material such as carbonate salts of alkali metals (K, Na, *etc.*) or naturally occurring dolomites or calcium/magnesium silicates (*e.g.*, olivine, serpentine) have been shown to produce higher gas yields with low tar and wax yields.^{30–34} Although tar cracking can be enhanced *via* the use of sorption-enhanced gasification, this process still requires high reaction temperatures (*e.g.*, >600 °C) and lower H₂ purity (30–50 mol%).^{22,35,36}

A novel thermochemical conversion technique which could be quite promising in the disposal of waste plastics commingled with biomass is alkaline thermal treatment (ATT), which uses alkali hydroxides (*e.g.*, NaOH, KOH, LiOH, *etc.*) as active materials to enhance the biomass conversion process.^{22,37} Previous research has shown that *via* this ATT reaction pathway, high purity H₂ (>90% v/v) can be generated from brown seaweeds at mild moderate temperature and pressures (<500 °C, 1 atm) while capturing evolved CO₂ in the form of alkali or alkali earth carbonate salts (*e.g.*, M₂CO₃, MCO₃).^{22,38–41} These salts offer deep capture potential of carbon dioxide due to their thermodynamic stability and ease of storage. Herein, alkaline thermal treatment (ATT) is studied in the context of converting a mix of plastic and brown seaweed in the presence of alkali earth hydroxides (*i.e.*, KOH and LiOH) and both pyrolysis and gas reforming catalysts (zeolitic materials and nickel-based catalysts, supported on ZrO₂).^{27,39} The main simplified reactions governing hydrogen production during the ATT reaction are given for an ethylene monomer of LDPE (eqn (1)) and a cellulosic monomer of brown seaweed (eqn (2)) below:²²

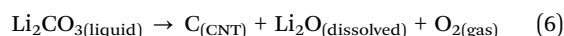


Electrochemical conversion of carbonate ions to high value carbon in molten salts

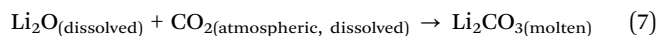
Previous studies have shown that regenerable molten salts can be used as liquid absorbents to facilitate both CO₂ and acid gas capture in a wide variety of modalities. The following electrochemical reactions generally proceed during electrolysis in molten lithium carbonate as the electrolytic material:^{42–45}



where eqn (3) is the formation of carbonate ions, eqn (4) is the four-electron reduction of the carbonate ions to carbon on the cathode, and eqn (5) is the continuous formation of oxygen on the anode. The production of carbon in the form of carbon nanotubes (CNTs) by electrolysis in Li₂CO₃ occurs together with the production of oxygen and lithium oxide given by:



Li₂CO₃ is consumed by the electrolysis and is continuously replenished by reaction of excess Li₂O (formed electrolysis product) with the CO₂ absorbed:

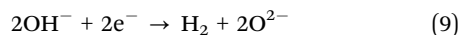
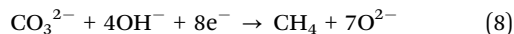


Capture of CO₂ (eqn (7)) enables carbon removal from the environment (*e.g.*, ambient air) by the molten salt. The subsequent electrolytic conversion of CO₂ to carbon (eqn (4)), and preferably to CNTs or graphene produces value-added products and potentially lowers the cost of the CO₂ capture and utilization.^{46,47} By using renewable electricity (*e.g.*, offshore wind), the overall process can be sustainable. Unfortunately, the melting of lithium carbonate that is necessary for carbonate ion formation (eqn (3)) occurs at the high temperature of 723 °C, whereas the decomposition of lithium carbonate and formation of lithium oxide (Li₂O) occurs at temperatures above 1200 °C. The presence of Li₂O from lithium carbonate is a condition for CO₂ capture by molten carbonates (eqn (7)).

Without the presence of metal oxides in the molten alkali metal carbonates, the capacity of the molten carbonates for capture of CO₂ from the environment is low, and therefore, the subsequent electrolytic CO₂ conversion to the value-added carbon products is limited in scale. The addition of Li₂O to molten lithium carbonate is restricted because dissolution of solid Li₂O in Li₂CO₃ is severely limited below *T* = 750 °C. When Li₂O is added to Li₂CO₃ at 750 °C, Li₂CO₃ is observed to absorb CO₂ from air; at 550 °C, Li₂CO₃ or its mixture with Li₂O is present in a solid form and Li₂CO₃ will disadvantageously lose (desorb) CO₂ into air by decomposition at that temperature.⁴⁸ Therefore, lithium carbonates cannot be utilized as reversible CO₂ sorbents at moderate temperatures below 750 °C. On the other hand, LiOH melts at 462 °C, possesses sufficient conductivity, and can act as an effective additive in the electrolysis processes.⁴⁹

Furthermore, the presence of molten LiOH can promote co-electrolysis of carbonates and H₂O to produce hydrogen and hydrocarbon fuels such as methane or longer-chain hydrocarbons given by the following cathodic and anodic reactions:⁵⁰

At cathode:



At anode:



These considerations, along with the potential role of LiOH in the alkali-mediated thermal conversion of biomass, guided our design of eutectic carbonates with lithium hydroxide as an additive.²² Here we define eutectic mixtures as compositions of lithium and sodium and/or lithium and potassium carbonate with melting temperatures significantly below those of the pure compounds. Such mixtures exist in a range of compositions and have been previously reported.^{51–54}

Carbonate ion reduction and carbon formation/deposition reactions from eutectic alkali metal carbonate melts in the 500–750 °C range have been reported to occur in the –0.8 to –1.9 V range of cathodic reduction potentials, with cathode materials comprising metals such as Ni, Pt, W, Ag, Mo, Al, Cu, steel as well as glassy carbon electrodes.^{55–57} Some carbon formation results were recorded on stainless steel electrodes (grade 304) in mixed melts comprised of Li₂CO₃–Na₂CO₃ or Li₂CO₃–K₂CO₃ blends (molar ratio, 62 : 38) at 650 °C.⁵⁸ Carbon was stated to be formed and the anodic peak at 1.5 V was attributed to carbon oxidation *via* the reaction:



No carbon production was observed at low current densities on a stainless steel electrode in molten Li₂CO₃–Na₂CO₃–K₂CO₃ at 600–700 °C.⁵⁹ However, carbon deposition did occur at high electrolysis voltages (–2.5 to –5 V) on stainless steel or mild steel electrodes in molten Li₂CO₃–K₂CO₃ at 540–700 °C and in Li₂CO₃, Li₂CO₃–Na₂CO₃ (eutectic mole ratio, 52 : 48) and Li₂CO₃–Na₂CO₃–K₂CO₃.⁵⁵ As an additional advantage in our salt composition design, Li–K carbonate has been shown to be a good catalyst for thermochemical conversion as shown previously.⁶⁰

Development of integrated thermo-electrochemical technology for the conversion of commingled marine plastic wastes and biomass into value-added products

The coupling of these two reactive conversion processes (*i.e.*, alkaline thermal treatment and carbonate molten salt electro-reduction) provides a novel and efficient way to address the problem of marine plastic wastes commingled with biomass, while allowing the production of high-purity H₂ and the utilization of seaweed carbon, which came from the atmosphere. The overall reaction can be considered a negative emission technology, particularly when renewable energy is used for the electrochemically driven elecATT reactions. Fig. 3 provides a

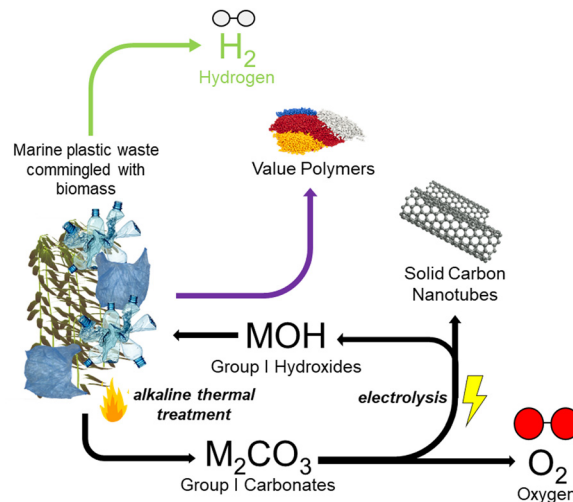


Fig. 3 Schematic showcasing the proposed theoretical tandem thermo-electrochemical (elecATT) method of producing value added products and high purity hydrogen from marine plastics commingled with biomass.

general diagram of the proposed tandem conversion thermo-electrochemical (elecATT) process which would be performed in a split-cell system, removing ash and other solid byproducts between ATT and electrolysis. The major components of the system include the thermochemical ATT of biomass and plastic wastes, which produces carbonate salts of K and Li and valuable volatile gases. These gases are then further converted (*i.e.*, cracked, reformed) into H₂ *via* catalytic treatment and a condenser is present to remove unconverted tars and recover waxes.²² Concurrent to these ATT processes, the molten carbonate salts are continuously converted into solid carbon, which deposits onto the cathode, and Li or K oxides.⁶¹ As the solid carbon is produced, the hydroxide is regenerated for the next cycle ATT reaction. Overall, this process represents an innovative thermo-electrochemical way to utilize complex marine waste streams.

Results and discussion

Alkaline thermal treatment (ATT) of plastic wastes and marine biomass with high water and salt contents

Novel hydroxide/carbonate molten salt system design for ATT reaction. Previous studies have shown that Group I hydroxides are more productive than Group II hydroxides at yielding H₂ during the ATT reaction.⁴⁰ Herein, a mixture of potassium hydroxide (KOH, Sigma-Aldrich) and lithium hydroxide (LiOH, Sigma-Aldrich) was chosen as the ideal salt mix as they can participate in the both the ATT reaction and electrochemical carbonate reduction. The mixtures of the resultant lithium and potassium carbonate salts form a low-melting system, which can serve as an electrolyte and carbon allows for the formation of solid carbon products (Fig. S4, ESI†).

For the electrochemical reactions, lithium carbonate (Li₂CO₃, ACS reagent, ≥99%), lithium hydroxide (LiOH, 98%) and potassium carbonate (K₂CO₃, ACS reagent, ≥99%) were all

obtained from Sigma Aldrich Chemical Co. A powdered blend of Li_2CO_3 (21.07 g, 0.285 mol) and K_2CO_3 (24.16 g, 0.175 mol) was ground at ambient temperature using mortar and pestle and was dried in air at 350 °C for 8 h in an electric oven. Following cooling, the resulting eutectic Li, K carbonate (62 : 38 mol ratio of lithium and potassium carbonates, nominal composition, $\text{Li}_{0.62}\text{K}_{0.38}\text{CO}_3$) was again ground and kept in a sealed container prior to the use. To prepare eutectic Li, K carbonate/lithium hydroxide blends, dried $(\text{Li}_{0.62}\text{K}_{0.38})_2\text{CO}_3$ was blended with LiOH , the resulting mixture was ground using mortar and pestle. The final blend was dried at 350 °C and then kept in a sealed container until further use. The use of lithium and potassium hydroxides for the ATT reaction would increase the reaction temperature, but they allowed the coupling of ATT and electrochemical carbonate reduction reactions in a single reactor system. Thus, we first investigated the hydrogen formation behaviors of the new hydroxide mixtures for the ATT reaction.

Bio-hydrogen production *via* ATT using molten salt hydroxide

Hydrogen production potential, total gas evolution (Fig. 4(a)), and the gaseous product slate (Fig. 4(b)) were analyzed for six distinct reactions involving alkaline thermal treatment (ATT) on brown seaweed (BS) alone, LDPE alone, and a 50:50 representative mixture of BS and LDPE and the results are compared to those of steam gasification (SG) cases. The ATT of BS alone using a eutectic mixture of LiOH and KOH offered advantages in both increased H_2 yield and the reduction of CO_2 emissions relative to SG of the same at 600 °C. This trend is supported by previous studies on the ATT of BS using Group I hydroxides.^{22,40}

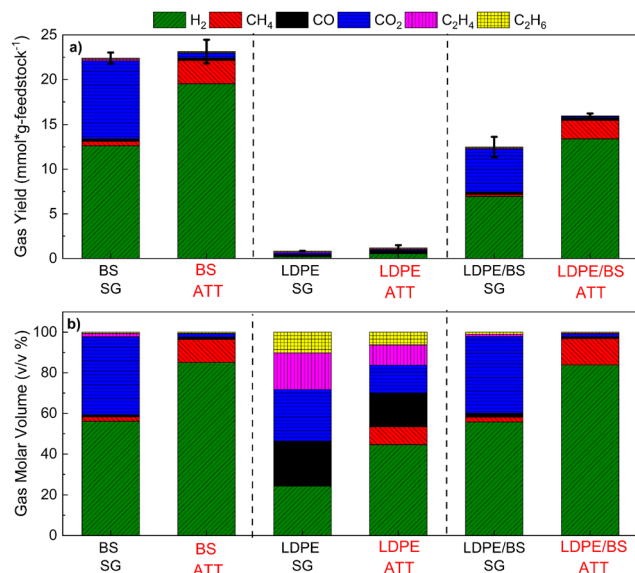


Fig. 4 Total gas yields (a) and gas component molar volume (b) obtained during the thermochemical steam gasification (SG) and alkaline thermal treatment (ATT) of brown seaweed (BS), low-density polyethylene (LDPE), and a 50 : 50 mixture of BS and LDPE. ATT was performed in the presence of a stoichiometric amount of the mixture of (Li,K)OH. Data is normalized to volume per gram ($\text{mmol g feedstock}^{-1}$).

For the ATT of LDPE alone at 600 °C, both low gas yield and low hydrogen production were realized, suggesting that the polymer participated only slightly in the SG and ATT reactions. This result was corroborated with the large percentage of solid waxy polymeric condensates obtained from the SG of LDPE at 600 °C, suggesting that the thermodynamic barrier for thermal cracking and gasification of LDPE is only slightly breached at 600 °C. Higher temperatures were not tested to prevent the undesired calcination of produced lithium and potassium carbonates, thus limiting the conventional gasification reactions. Auto-decomposition of the Li–KOH mixture was performed in the absence of biomass or plastic, revealing minimal H_2 yields compared to the actual ATT reactions (Fig. S10, ESI†).

In the SG and ATT of LDPE and BS mixtures, a similar trend was observed, where the use of ATT was able to increase the hydrogen yield of the reaction by approximately 93% and carbon dioxide emissions were reduced by up to 97%. These results suggest that ATT of marine biomass commingled with plastic wastes could be used as a feedstock to produce relatively pure H_2 (84%) gas with enhanced carbon capture through the production of stable carbonate salts (*e.g.*, lithium and potassium carbonate).

Due to the absence of hydroxides during steam gasification, water is the main oxidant. The gas evolution, cracking, reforming, water gas shift, and steam methane reforming reactions are all correlated to temperature.⁶² Additionally, tar and residue cracking and reforming also follows the same behavior.⁶² In order to probe the temperature effect on total gas yield, co-SG and co-ATT of LDPE/BS were performed at 500 °C as well (Fig. 5). With respect to the previously reported data obtained at 600 °C, an increase in the reaction temperature by 100 °C results in an increase in the total gas yield by almost 268%, with significant increases in H_2 and CO_2 . However, comparison of the ATT gas yields of the same feedstocks at 500 and 600 °C reveals almost comparable total gas yields and gas compositions, since most of the ATT reactions have already occurred at a moderate reaction temperature of 500 °C.

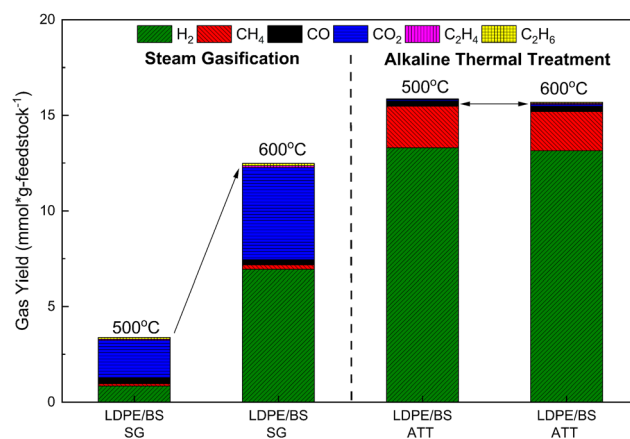


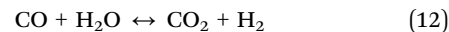
Fig. 5 Total gas yield and gas distribution from steam gasification (SG) and alkaline thermal treatment (ATT) of a mixture of BS and LDPE (50 : 50) at both 500 and 600 °C.

(Fig. 5). This behavior highlights the distinct energetic and conversion advantages offered by ATT with respect to steam gasification in the thermochemical processing of carbonaceous feedstocks; ATT could be used to lower the energetic requirements of hydrogen production while capturing carbon.⁶³ It is also important to note that, the gasification process requires dried feedstock, whereas wet and salty feedstocks (*e.g.*, marine plastic wastes comingled with seaweed) can be used directly in an ATT reactor without any pre-treatment or drying, which is one of the most important benefits of the ATT technology.

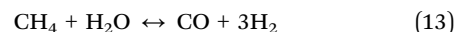
Investigation of different gas formation mechanisms during ATT of seaweed, plastic and their mixture using molten salt hydroxide

As shown in Fig. 6, H₂ evolution involves multiple reaction pathways and mechanisms occurring at different temperatures. H₂ is formed more rapidly and at earlier temperatures in ATT than in SG (Fig. 6(a)–(c)). In the case of the ATT of BS and the ATT of LDPE/BS, four distinct H₂ peaks can be observed from the kinetic graphs, starting as early as 150 °C and reaching a maximum rate of 0.6 mmol min⁻¹ g feedstock⁻¹ with both systems. Hydrogen evolution during ATT ceased at about 500 °C (as indicated by a return to the baseline), whereas during conventional SG, hydrogen evolution did not occur significantly

until at least 550 °C. Relatively no CO₂ evolution was observed in the case of ATT due to the capture of CO₂ into carbonate salts as given by eqn (1) and (2). The capture of CO₂ also helped to boost H₂ production by shifting the thermodynamic equilibrium of the water gas shift (WGS) reaction, as given below:



According to La Chatelier's principle, the consumption of CO₂ *via* reaction with LiOH and KOH will shift the equilibrium of the WGS reaction towards the right. Thus, ATT is inherently productive in increasing H₂ production while also producing virtually no gaseous CO₂ emissions.^{22,38} In both the ATT of BS and the ATT of LDPE/BS mixture, methane production increased approximately 5.3-fold relative to SG (Fig. 4 and 6). This is likely due to the enhancement of methanation reactions (*e.g.*, CO + H₂ ↔ CH₄ + H₂O) and elevated light gas reforming and tar cracking, increased by the presence of the hydroxide mixture.³⁸ Results suggest that significant methane evolution during ATT occurs at about 380 °C and returns to the baseline at about 500 °C (accompanied by H₂ Fig. 6(a) and (c)). Increased methane production during ATT suggests more efficient conversion of light gases and possible enhanced tar and wax cracking. Previous results suggest that catalysts (such as nickel catalysts) can enhance the conversion of methane to lighter gases during ATT *via* steam methane reforming (SMR) as given by eqn (13):^{22,37,39}



Catalytic enhancement of the ATT process increasing H₂ yield and purity

Catalysts can assist with the cracking and degradation of carbonaceous feedstocks (*e.g.*, plastics, biomass) during thermochemical reactions in both the solid and gaseous states.^{22,27,64} They can also assist with reforming reaction which can boost the overall amount of hydrogen in the final product.⁶⁵ Such catalysts include Ni-based systems and zeolitic materials. As previously shown in Fig. 6(b), the SG and ATT of LDPE alone yielded low H₂ evolution compared to the ATT of BS. Thus, in an effort to improve the ATT conversion efficiencies of plastics at lower pressures and temperatures than conventionally used a catalyst system of Ni supported on ZrO₂ mixed with γ -zeolites (30 : 1 Si/Al ratio, ZLT) was used in both *in situ* and *ex situ* configurations. As shown in Fig. 7(a) and (b), using either Ni/ZrO₂ or γ -ZLT *in situ* during ATT of LDPE alone increases the H₂ yield by approximately 267%. The combination of the two catalysts proved to be quite promising for enhancing the hydrogen yields from the ATT of LDPE, producing over 820% more H₂ during *in situ* Ni/ZLT catalytic ATT (catATT) and over 1242% more H₂ during *ex situ* Ni/ZLT catATT (Fig. 7(b)). Additionally, during the catATT reactions of LDPE, no observable waxy condensate product was found after the reactions. This suggests that the catalysts are directly assisting with the conversion of the plastic feedstock.⁶⁶

Previous work from our group has shown that catalysts for ATT perform similarly whether they are present *in situ* or

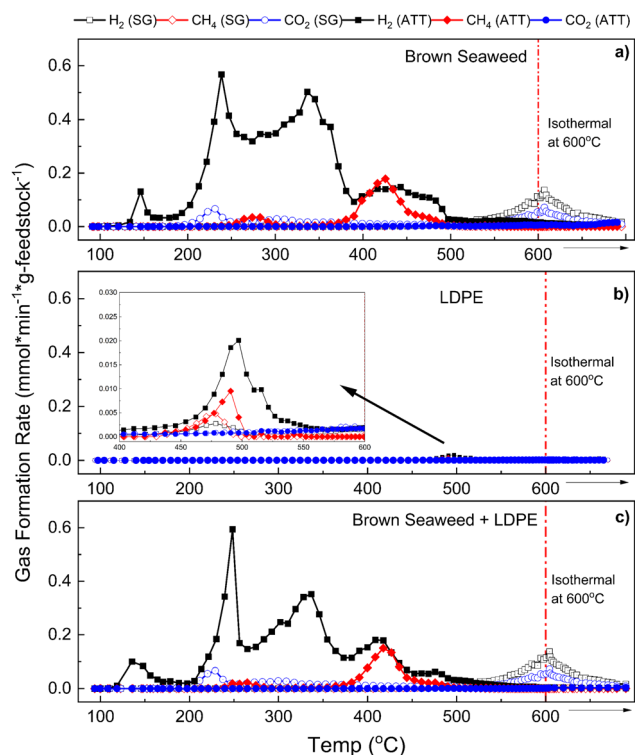


Fig. 6 Kinetic data for gas evolution of the main reaction gases, H₂, CH₄, and CO₂, produced during the thermochemical steam gasification (SG) and alkaline thermal treatment (ATT) of BS (a), LDPE (b), and a 50 : 50 mixture of BS and LDPE (c). Open circles represent the SG reaction kinetic data whereas closed circles represent the ATT reaction kinetic data. Kinetic data are expressed as gas formation rate per minute per gram (mmol min⁻¹ g feedstock⁻¹).



Fig. 7 Catalytic alkaline thermal treatment (CatATT) of LDPE using a zeolite catalyst (ZLT), a nickel catalyst on zirconia (Ni), and a combination of the two (Ni/ZLT) both *in situ* and *ex situ*. (a) Gas formation kinetics of LDPE ATT with a 1:1 mixture of Ni/ZLT catalysts both *in situ* (closed shapes) and *ex situ* (open shapes). (b) Total gas yield and distribution of LDPE ATT reactions with *in situ* catalysts (Ni, ZLT, and a 1:1 mixture of the two) and *ex situ* catalysts (a 1:1 Ni/ZLT mixture).

ex situ.^{39,67} In both cases they assist in the promotion of the steam methane reforming (SMR – eqn (13)) and water gas shift (WGS – eqn (12)) reactions, which is also observed herein in the case of catATT of LDPE. CO₂ is produced during the SMR reaction, as can be seen in the case of LDPE catATT *ex situ* (Fig. 7(b)) and is present in the final gas product if no downstream scrubbers are used. During *in situ* catATT, this CO₂ is captured by excess hydroxides, forming additional carbonate materials, which results in a higher quality of hydrogen. However, from a process standpoint, utilizing *in situ* catATT may pose challenges with catalyst recovery and regeneration due to the caustic environment of eutectic salts. This effect can be observed in the post reaction analysis of the catalysts by PXRD (Fig. S11, ESI†) and SEM (Fig. S12, ESI†), showing salts caked onto the catalysts in the case of *in situ* catATT. As shown by Stonor *et al.* (2017),³⁹ it may be useful to use Ca-rich materials to capture CO₂ produced from the SMR downstream of the *ex situ* catalyst to boost the quality of H₂ gas back to near 99%.

Finally, this catalytic nickel/zeolite system was extended to the ATT of a 50:50 mixture of LDPE/BS to realize any potential conversion advantages between catATT and conventional ATT/SG at 600 °C. *In situ* catATT of LDPE/BS yielded 61% more H₂ and *ex situ* catATT of the same yielded 89% more H₂ than conventional ATT (Fig. 8(b)). Kinetically, *ex situ* catATT of LDPE/BS shows three distinct H₂ evolution peaks (at ~250 °C, 340 °C, and 440 °C) while *in situ* catATT of LDPE/BS shows one sharp peak (at 260 °C) and then a broad H₂ evolution peak ending close to 600 °C (Fig. 8(a)). This difference points to the stronger gas phase activity of the Ni/ZLT catalytic mixture, performing cracking, gas reforming, and WGS reactions simultaneously, as supported by previous work.^{22,40}



Fig. 8 CatATT of a mixture of BS and LDPE with a Ni/ZLT catalyst system both *in situ* and *ex situ* at 600 °C with both kinetic gas yield data (a) and total gas yield data (b).

Fate of seaweed and plastic waste carbon through the ATT reactions

Analysis of the waxy condensates. Waxy solid condensates were easily recovered during the SG and ATT of LDPE samples *via* the condenser trap. FTIR confirmed that the organic chemical composition of the plastic condensates was quite similar (Fig. S9, ESI†). Distinct peaks were observed at 2920–2850 (C–H alkane stretching), 1460 (C–H methyl bending), and 720 cm⁻¹ (methylene “rocking” vibration).⁶⁸ This suggests that the waxy condensates almost certainly come solely from the plastic starting materials and that the rough chemical composition of the waxes does not differ much from the original material. Differential scanning calorimetry (DSC) revealed that the crystalline structures of the waxy solid condensates were altered with respect to virgin LDPE.

Melting and cooling curves for all the samples tested shifted lower, such that the crystallization temperature (T_c) of the waxes was in the range of 76.3–83.2 °C (*vs.* 93.0 °C for virgin LDPE) and the melting temperature (T_m) was in the range of 84.3–88.9 °C (*vs.* 110.8 °C for the virgin LDPE) (Fig. 9(a), (b) and Table S1, ESI†). Percent crystallinity (X_c) was also calculated based on the extracted enthalpies of melting and using a reference enthalpy of melting for pure crystalline PE (see eqn (22)).⁶⁹ In the case of the wax from the LDPE SG reaction, X_c was 6.9% lower than for virgin LDPE, whereas LDPE/BS SG wax had an X_c which was only 1.0% lower than that of virgin LDPE. Interestingly, the wax from ATT of LDPE/BS has a X_c of 61.0%, 5.8% higher than that of virgin LDPE (Fig. 9(a), (b) and Table S1, ESI†). This suggests that the presence of wet and salty biomass during the reaction can potentially lessen the thermochemical damage of the reactive process, producing a more crystalline waxy condensate. In the case of the ATT waxy condensates, the increase in percent crystallinity could be a result of the interactions of the alkaline salts and the melting/pyrolyzing plastic. Although the crystallization and melting points have been shifted for these



Fig. 9 Differential scanning calorimetry (DSC) data on the solid waxy condensable products from both SG and ATT reactions to compare the efficacy of the crystallization and melting behaviors of the polymeric products with respect to the original LDPE. DSC heating curves (a) and cooling curves (b) were collected in argon atmospheres for SG of LDPE, SG of LDPE/BS, and ATT of LDPE/BS. The salt from the latter ATT reaction (LDPE/BS ATT) was tested for residual polymeric matter.

waxes, the relatively similar and even enhanced crystallinities suggest that these waxy condensates could be feedstocks for plastic production operations or blending into existing polymer supply chains, allowing the recovery of valuable materials from detritus plastics commingled with marine biomass.

Gel permeation chromatography (GPC) analysis of the waxy solid condensates revealed that M_n (number average molecular weight) was reduced significantly when compared with the virgin LDPE (Fig. 10(a), (b) and Table S2, ESI[†]). The longer retention time and narrowing of the elution curve for the LDPE SG Wax, LDPE/BS SG Wax, and LDPE/BS ATT Wax suggests that the thermochemical processing of these plastics at 600 °C, either by steam gasification or ATT, alters the polymeric structure through melting and volatilization and then subsequent recrystallization with shorter fragmented polymers and modifications to the LDPE branching. This drastic change can also be exemplified by the change in the dispersity index (*i.e.*, M_w/M_n) between the original LDPE polymer and the post-reaction waxy condensates which dropped from 3.61 to values between approximately 1.16–1.59. Lower dispersity values indicate more polymeric uniformity, which is likely a result of the thermochemical cleavage and reorientation of LDPE side chains during the SG/ATT reactions.

Previous studies have suggested that more uniform polymers with dispersity indexes closer to 1 and lower M_n values are easier to process in polymeric engineering systems, such as extruders, due to lower shear stress susceptibility.⁷⁰ As a follow-up, a sample of final molten ATT salt was tested as a proof of concept (*via* DSC, GPC) to probe any residual plastics remaining in the salt mixture. As shown in Fig. 9(a), (b) and 10(b), no detectable melting of the ATT salt reaction product was

observed *via* DSC and minimal elution was detected from the salts *via* GPC, respectively. The exception was the salt of the LDPE ATT reaction, which showed minor polymeric residues present, likely due to the pure feedstock of the reaction existing as plastic. These results suggest that high purity, lower molecular weight polymers with similar crystallinities as the starting LDPE material could be easily recovered during these thermochemical reactions.

Distribution of carbon in different ATT product streams and characterization of formed molten carbonates/hydroxides

Analysis of the reaction intermediates revealed that ATT increases the percentage of carbonates with respect to all the feedstocks tested at 600 °C (Fig. 11(a)). The percentage of inorganic matter in the solid product was 97.5% in the case of BS ATT, 72.1% in the case of LDPE/BS ATT, and only 28.5% in the case of LDPE ATT. Visually, the presence of carbonate products can be seen by the change in the reaction product from a black material to a white powder (insert photo, Fig. 11(a)). This qualitative result suggests ATT allows increased carbon conversion by increasing char cracking and offsetting any potential char formation *via* solid carbonate salts. The low percentage of inorganic carbon in the solid phase of LDPE ATT is likely due to low feedstock conversion efficiencies in the absence of catalyst at 600 °C and potential salt/plastic interaction issues. This was further corroborated by the amount of solid waxy condensate products produced during the ATT of LDPE samples. As shown by the full carbon distribution balance (Fig. 11(b)), a high percentage of waxy solid was recovered in the condenser trap in the LDPE SG and LDPE/BS SG cases. Combustion analysis confirmed that it was a carbonaceous material, with a similar percentage of carbon as the original feedstock (~85 wt%). This suggests that a portion of the carbon is not being fully converted in the case of either LDPE

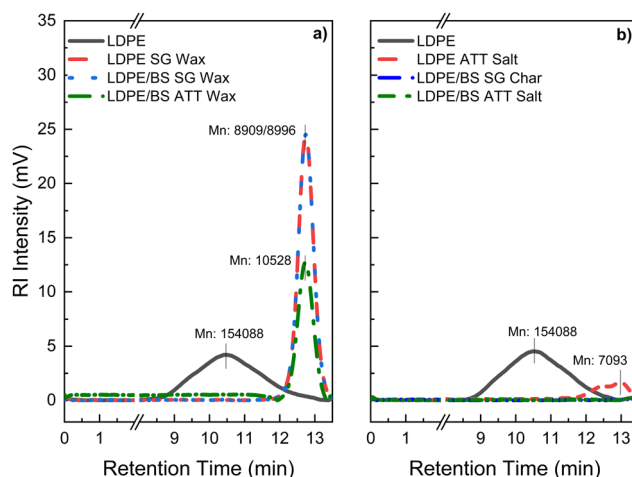


Fig. 10 High temperature gel permeation chromatography (HT-GPC) elution curves expressed in refractive intensity (RI) of the waxy condensate products of SG and ATT reactions involving LDPE (a) and the corresponding reaction salt mixtures (b) both run at a steady state temperature of 140 °C using 1,2,4-trichlorobenzene (TCB) as a solvent.

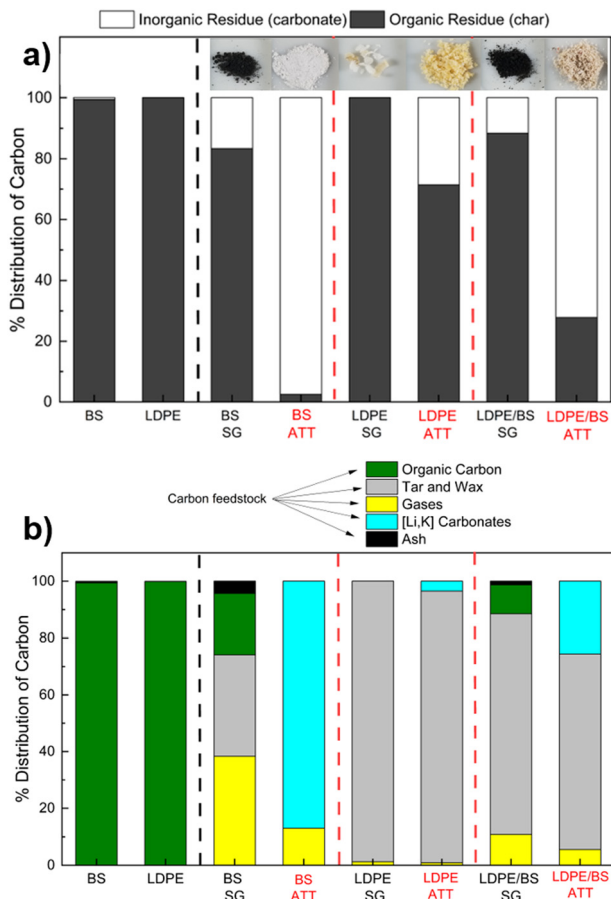


Fig. 11 (a) Carbon distribution from the solid products (*i.e.*, char or salt) of the various reactions studied in terms of inorganic residues (carbonates) and organic residues (chars). (b) Carbon distribution of all the thermochemical reaction products from both SG and ATT cases of BS, LDPE, and a 50 : 50 mixture of BS and LDPE are shown. The products are classified as organic carbon (char, solid residues), tar and wax (solid and liquid condensables), gases (CO , CO_2 , C_2H_4 , C_2H_6), (Li, K) carbonates (inorganic carbon, solid residues), and ash (non-combustible solid residue).

or LDPE/BS SG/ATT without the presence of the previously discussed catalytic system. However, ATT is still an effective method to not only perform thermochemical conversion at lower temperatures but also allows for the offset of potential carbon emissions during the reaction through the formation of solid carbonate salts.

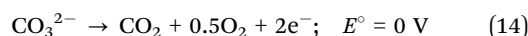
Integration of molten salt electrolysis to develop elecATT technology directly converting carbonates into solid carbon

Carbonate reduction mechanisms during molten salt electrolysis of elecATT products. Representative cyclic voltammograms are given in Fig. 12 for molten salt solutions in the presence and absence of CO_2 with a galvanized steel electrode. Here, CRE denotes the Carbonate Reference Electrode (standard potential *vs.* reference CO_2 oxidation reaction is $E^\circ = 0 \text{ V}$), which was confirmed in our control experiment conducted under air purge, as the standard potential of 0 V characteristic of the carbonate ion oxidation in molten carbonates was

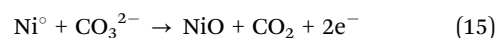


Fig. 12 Representative cyclic voltammograms (CV) of a galvanized steel cathode in molten carbonate and lithium hydroxide blend (initial blend composition: Li_2CO_3 : K_2CO_3 : LiOH , 52 : 32 : 15 molar ratio). Anode: nickel crucible; temperature: $550 \text{ }^\circ\text{C}$. The potential scan started cathodically from 0 V, and the reduction and oxidation sweep directions are shown by arrows (IUPAC convention). Solid and dotted lines show three consecutive scans (scan rate, 20 mV s^{-1}) measured under nitrogen and CO_2 purge, respectively. Designations A and C stand for *anodic* and *cathodic* peak potentials, respectively.

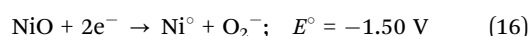
observed.^{71,72} The carbonate ion oxidation reaction is indicated by A1 in Fig. 12 and given as



The observed formation of black coating on the anode interior (see Fig. S6, ESI†) is attributed to the nickel oxidation reaction (reported standard potential $0.697 \text{ V}^{71,73}$) on the anode-melt interface:



The oxidation peak potential (eqn (15)) is indicated by A2 in Fig. 12 on the oxidation scan under a nitrogen atmosphere. Numerous prior studies reported a variety of reduction reactions for nickel compounds in the presence of neutral gas or carbon dioxide:^{74–77}



During the cathodic reduction, at potentials in the -1.5 to -1 V range, nickel oxide dissolves, forming complexes of nickel and carbonate ions. These complexes are reduced to nickel and carbonate ions (designated by C2 in Fig. 12); the formed nickel is then oxidized in the following anodic scan, at potentials in the 0.5 to 0.9 V range.⁷⁶ Under a CO_2 atmosphere, the oxidation peaks A2 are broadened and shifted to lower oxidation potentials due to the formation of complexes between dissolved nickel ions and dissolved CO_2 .

In our experiments with the eutectic carbonate–LiOH blends in nitrogen atmosphere (Fig. 12), carbon was produced by cathodic reduction of the carbonate anions (eqn (4)); indicated as C1 in the -2.3 V range – Fig. 12). The peaks C1 were

prominent due to high concentrations of the carbonate CO_3^{2-} anions formed by dissociation of the molten alkali metal carbonates. Carbon was deposited on the galvanized steel cathode in significant quantities, along with deposition of the alkali metals. Electroreduction processes in eqn (4) (C1 in Fig. 12) can be seen as transient, as the corresponding peak potentials decreased with increasing number of scans, indicating that the majority of the dissolved CO_2 and carbonate ions were electro-reduced.

The reactions in the electrodeposition of carbon by CO_2 electrolysis are important for generation of value-added carbon products in our hybrid process.^{78,79} In our experiments with the molten Li, K carbonate and LiOH blends under a nitrogen atmosphere (Fig. 12), carbon was produced by cathodic reduction of the carbonate anions formed by dissociation of the molten alkali metal carbonates (indicated as C1 in the -2.3 V range; Fig. 12). Carbon deposited on the galvanized steel cathode in significant quantities depending on the molten salt composition, as outlined below. It should be noted that carbon formed on the cathode can be re-oxidized on the anode at higher potentials (transient reactions indicated by A3 in Fig. 12).^{80–82}

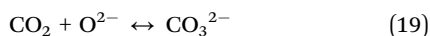


Effect of lithium concentration on carbon yield in electro-splitting

Coulombic efficiency (C_e , %) was calculated as the percent of applied current charge that resulted in carbon production according to eqn (18):⁸³

$$C_e(\%) = 100 \times \frac{M_{\text{experimental}}}{M_{\text{theoretical}}} \quad (18)$$

where $M_{\text{experimental}}$ is the mass of washed carbon product removed from the cathode; $M_{\text{theoretical}} = (Q/nF) \times (12.01 \text{ g C mol}^{-1})$ is the theoretical mass, which is determined from Q , the time integrated charge passed during the electrolysis; $F = 96485 \text{ A s mol}^{-1} \text{ e}^-$, the Faraday constant, and $n = 4 \text{ e}^- \text{ mol}^{-1}$, reduction number of tetravalent carbon. Previous results indicate that both high initial concentrations of carbonate ions (CO_3^{2-}) and lithium in the molten electrolyte are required for the efficient conversion of CO_2 into carbon, according to the well-established mechanism of the 4-electron reduction of the carbonate ions to carbon (eqn (4)).⁷⁸ For the reaction to occur in the molten electrolyte, a certain equilibrium concentration of the carbonate ions should be established, either by eqn (19) or by the formation of carbonates during ATT:⁶¹



Our results (Fig. 13) demonstrate that the effect of LiOH addition to the eutectic blend of two molten carbonates is the additive result of two opposing trends. That is, the enhancement of the overall lithium content in the composite by approximately 1 wt% at $C_{\text{LiOH}} \sim 15$ mol% enables approximately 20% enhancement in the carbon product yield and Coulombic efficiency (Fig. 13). However, further “dilution” of the carbonate by LiOH and decrease in $C_{\text{carbonate}}$ leads to a

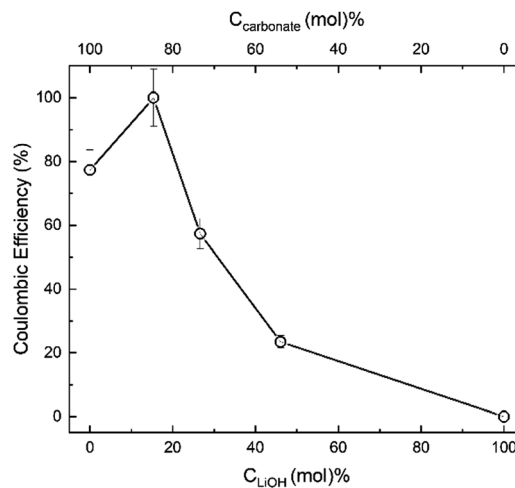
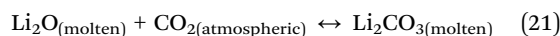
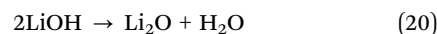


Fig. 13 Effect of initial LiOH content (C_{LiOH} , mol%) and initial carbonate content ($C_{\text{carbonate}}$, mol%) of the $\text{Li}_2\text{CO}_3/\text{K}_2\text{CO}_3/\text{LiOH}$ electrolyte on the Coulombic efficiency of CO_2 electro-splitting process at 500°C . The electrolyte $\text{Li}_2\text{CO}_3/\text{K}_2\text{CO}_3$ mol ratio was set at eutectic 1.63 throughout.⁵¹

precipitous drop in the production of carbon (Fig. 13 and eqn (4)), with the initially pure LiOH electrolyte failing to result in any carbon formation under the conditions of our experiment. Molten LiOH fails to produce enough CO_3^{2-} in our experiments in the allotted timescale because the CO_2 capture occurs *via* the following sequence of reactions, which are both kinetically slow and thermodynamically challenging:⁸⁴



Deng *et al.* demonstrated that it is the presence of lithium carbonate that affords the electrochemical conversion of CO_3^{2-} to C (eqn (4)), *via* formation of the carbonate ions (eqn (3)).⁸⁴ Hence, LiOH added to the carbonate melt must produce Li_2O that can absorb CO_2 due to its strong alkalinity, resulting in a continuous conversion of CO_2 to carbon on the cathode (eqn (4)) and oxygen on the anode (eqn (5)).

It has been demonstrated that the carbonation of Li_2O (eqn (7)) is of vital significance as a key intermediate reaction of carbon formation.⁸⁴ Since Li_2O serves as the intermediate for CO_2 capture and electrochemical conversion and no Li_2O is initially present in LiOH, no deposition of carbon from the LiOH melt occurs (Fig. 13).⁷⁸ The rate of carbonation (eqn (7)) should match the rate of electrochemical deposition (eqn (4)) to achieve a net transformation of CO_2 . It appears from our electro-splitting results (Fig. 13) that the carbon (CNT) formation was determined by the initial concentration of carbonate (displaced by LiOH) and not by the mass of CO_2 absorbed.

Electrolyte materials-characterization

Powder X-ray diffraction (PXRD) was performed on the products of CO_2 electrolysis collected on galvanized steel cathodes (Fig. S8, ESI†). Broad peaks centered at $2\theta = 26 - 26.2^\circ$ were

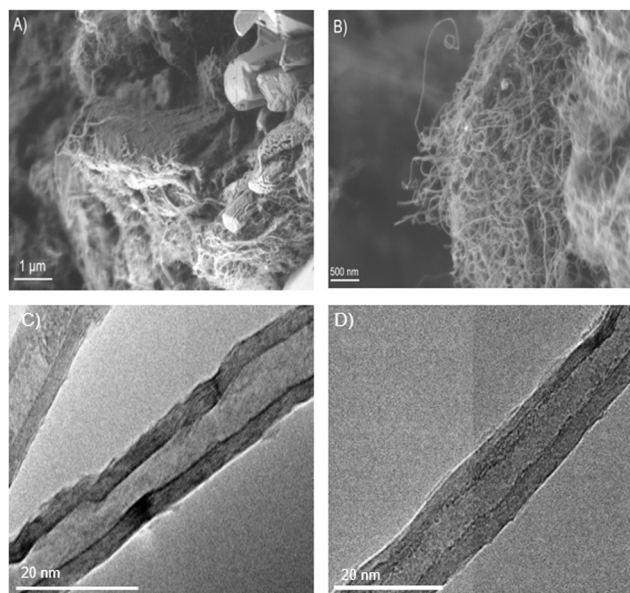


Fig. 14 Top row: Representative SEM images of product obtained by electrolyzing $(\text{Li}_{0.62}\text{K}_{0.38})_2\text{CO}_3$ + 13 mol% LiOH with 8 wt% LDPE at 14.2k \times magnification (A) and 20.2k \times (B). Bottom row: Representative TEM images of product obtained by electrolyzing $(\text{Li}_{0.62}\text{K}_{0.38})_2\text{CO}_3$ + 13 mol% LiOH with 8 wt% LDPE (C) and the same with 8 wt% seaweed (D), confirming multiwalled carbon nanotubes.

prominent in XRD patterns of the electrolysis products. The product collected from the cathode at the end of the hybrid process was purified and subjected to elemental analysis for carbon content. We were able to obtain a product that contained up to 90–98 wt% carbon; weighing the products enabled calculation of the Coulombic efficiency of the CO_2 electrolysis, which was close to 100%, both with LDPE and brown seaweed (BS) initially present. Concentrations of lithium, zinc and nickel in the purified products of the hybrid process with LDPE and BS varied (0.1–0.5 wt%, 0.01–0.03 wt%, and 0.1–0.5 wt%, respectively). Interestingly, the peaks at around 26.2° were clearly present in the products wherein LDPE was initially present, but were minor or absent in the products that originated from the seaweed-containing blend. That indicated that the latter products contained primarily amorphous carbon. However, carbon nanotubes were observed in both types of products.

The XRD patterns of the electrolysis products also featured peaks at $2q = 21.3^\circ$, 30.6° , and 31.8° , characteristic of the lithium carbonate admixtures that were not removed from the products in the process of purification.^{85,86} XRD pattern peaks at 34.4° and $2q = 34.4^\circ$ and 36.2° were due to the presence of ZnO nanoparticles (standard JCPDS cards #79-0206, #36-1451), formed *via* oxidation of zinc originally present on the galvanized steel cathode surface.^{87,88} Finally, peaks that are present in some products at $2q = 43.5^\circ$ and 44.7° are due to NiO crystal lattice and Ni electrodeposited onto the product on the cathode from the molten salt solution, respectively.^{88,89} It has been noted previously that zinc and nickel ion admixtures to the molten carbonates mediate the synthesis and

contribute to the yield of carbon nanotubes in the process of CO_2 electrolysis.^{47,53,90}

Analysis of the carbon nanotube (CNT) products

SEM and TEM confirmed the presence of CNT products in the electro-reduced product salt, as deposited on the cathode (Fig. 14). SEM allowed the visualization of the CNT microfibers from the electrolysis of the $(\text{Li}_{0.62}\text{K}_{0.38})_2\text{CO}_3$ salt with 13 mol% LiOH, while TEM showcases the multiwalled structures (Fig. 14(A)–(C)). SEM was unable to confirm the bulk presence of CNTs in the same reaction done with BS, however TEM showcased that multiwalled CNTs were indeed present in the post-reaction mixture (Fig. 14(D)). This corroborates the XRD data (Fig. S8, ESI[†]), which indicated a higher degree of amorphous carbon based on the graphitic peak at 26.2° .

Great potential for offshore marine plastic waste cleanup applications

One of the most pressing issues relating to the abundance of marine plastic debris present on the ocean surface and top ocean strata is the volume it occupies because of its relatively low density.⁴ One option for treatment of these marine and coastal plastic wastes is simply harvesting and then subsequent landfilling. There are a few companies already involved in plastics cleanup, such as The Ocean Cleanup[™], which utilizes a process involving the booming of the ocean in high wind and entrance points.⁹¹ However, these solutions require landfilling of the collected debris which will simply transfer the problem from sea to land, although in a more controlled manner. Furthermore, anaerobic decomposition of commingled biomass in landfills results in emission of methane, a potent greenhouse gas. The disposal of these marine plastics commingled with biomass *via* thermo-electrochemical processing is highly advantageous as it not only enables production of high-value products from detritus feedstocks but also allows the volumetric reduction of the feedstock. It is essentially a “carbon-concentrating” mechanism that allows for upgrading, capturing, and then deposition of carbon in the form of CNTs. The overall estimated volumetric reduction using the known densities of the reactants and products is approximately 220% (Fig. S3, ESI[†]).^{10,17} This makes the elecATT tandem thermo-electrochemical treatment (proposed in Fig. 3) of waste streams a highly attractive method to generate energy, high-value products, and reduce the relative volume the waste occupies.

Conclusions

In this work, we successfully demonstrated the thermo-electrochemical conversion of LDPE commingled with wet and salty seaweeds into high purity H_2 , valuable waxy polymeric condensates, and high-value CNTs. Ni/ZrO₂ and zeolite catalysts were able to increase the production yield of H_2 from LDPE by approximately 1242%. The recovery of uniform high-purity waxy condensates from the SG and ATT of LDPE and LDPE/BS was confirmed by similar % crystallinities, melting

curves, and resultant size-exclusion column elution data. Carbon analysis showcased that the formation of carbonates was prevalent in the case of ATT of brown seaweed and LDPE mixed with brown seaweed; however, negligible carbonate formation was observed in the ATT of plastic alone (LDPE), confirmed by low gas yields *via* Micro GC analysis. This elucidates that the direct thermochemical conversion of LDPE at 600 °C is poor, and thus catalytic enhancements are needed should the reaction be carried out at moderate temperatures. Finally, the electroreduction of the eutectic lithium/potassium carbonate mixture proved successful, yielding up to nearly 100% of high purity CNTs, as confirmed by cyclic voltammetry, SEM, and XRD of the post-reaction mixtures. These results suggest that tandem thermo-electrochemical reaction systems can create high value products from environmental pollutants, such as biogenic materials commingled with marine plastic wastes, through the concentration of carbon and feedstock volumetric reduction. Additionally, the use of solar or solar thermal systems to heat the reactor up to molten salt temperatures in addition to utilizing renewable electricity for the electro-reductive hydroxide regeneration both have a great potential within this novel ocean-based Bio-energy with Carbon Capture and Storage (BECCS) and marine waste treatment and upcycling technology.

Experimental

Materials

Feedstocks. Brown seaweed (*Saccharina japonica*) from the coastal waters of Wando Island, Korea was utilized for this study, with a total solid ash content of 28.3 wt% and a moisture content of 7.8 wt%.²² The seaweed was ground to a particle size of less than 150 micrometers. Alkaline thermal treatment is capable of processing wet biomass samples, but for ease of storage the seaweed was sun dried and rehydrated during the experiments. For the representative plastic species, polyethylene powder (<500 micron, 99% pure, Alfa Aesar) was utilized due to its major presence as a marine surface plastic pollutant (Fig. 1 and Fig. S2, ESI[†]) with a reported carbon content of about 85 wt%.²²

ATT catalysts. To enhance the conversion potential of the feedstocks studied, a zeolite catalyst (γ -zeolite SiO₂-Al₂O₃, 30 : 1 Si/Al mole ratio, 780 m² g⁻¹, Alfa Aesar) and a nickel-based catalyst (10 wt% Ni supported on zirconia, prepared in-house) were studied both *in situ* and *ex situ*. The nickel catalyst was prepared in-house using nickel(II) nitrate hexahydrate dissolved in ethanol and impregnated on zirconia *via* gradual heating and addition of ZrO₂ following the methodology of Zhang *et al.* (2020).²² Afterwards, the particles were dried at 70 °C overnight and calcined in air for 3.3 hours. Finally, the catalysts were then reduced in a hydrogen atmosphere for final activation.²² Characterization of the raw catalysts and the catalysts after both the *in situ* and *ex situ* LDPE ATT were performed using PXRD (Fig. S11, ESI[†]) and SEM (Fig. S12, ESI[†]) to assess any structural or visual changes to the catalysts.

Methods

ATT reactions. The ATT reaction was performed in a horizontal quartz furnace reactor (2.54 cm O.D. × 56.00 cm in

length, Mellen Co., SC12R) using nitrogen as a carrier gas. The solid feedstocks with the hydroxide salts were loaded into the isothermal region of the furnace. A thermocouple was installed in the reactor to monitor the temperature of the reaction. Water was injected at a flow rate of 0.023 mL min⁻¹ in the preheat furnace operated at 300 °C to provide the steam for the reaction. The gaseous products were evaluated using a Micro GC (Inficon 3000) with multiple channels to capture components from H₂ to ethylene/ethane, allowing both kinetic and total yield data to be established. H₂, O₂, N₂, CH₄, and CO were detected using two 10 m Molsieve columns, and CO₂ and C₂H₆ were detected using an 8 m Plot U polymer column. For the various reactions, 250 mg of feedstock, either brown seaweed (BS), LDPE, or a combination of BS and LDPE was loaded into a 15 mL ceramic boat and placed in the center of the horizontal reactor.

Three main types of reactions were performed: steam-gasification (SG), ATT, or catalytic-ATT (catATT; either *in situ* or *ex situ*). For SG reactions, the ceramic boat was charged with feedstock and no salts were added. For ATT reactions, the corresponding amount of a hydroxide mixture (LiOH : KOH, 50 : 50 molar ratio) was added to the ceramic boat, as determined by stoichiometric calculations (stoichiometry given by eqn (1) and (2); two molar equivalents of hydroxide was used per mole of carbon). Finally, for catalytic-ATT reactions, γ -zeolite and Ni/ZrO₂ and a 50 : 50 mixture of the two were charged in the ceramic boat at a ratio of 1 : 1 feedstock : catalyst (w/w) along with the feedstock and salt (*in situ*), or placed in a steel wool chamber ~20 cm downstream of the ceramic boat (*ex situ*). This ratio of brown seaweed (BS) to LDPE (1 : 1) was chosen as a representative metric for the commingling of marine waste and biomass. The reactor was continuously filled with a carrier gas, N₂, at a constant rate of 50 mL min⁻¹ as measured by a mass flow controller (Omega FMA5508). The reactor was preheated at a rate of 4 °C min⁻¹ to 80 °C, at which point the temperature was maintained for 30 minutes. Afterwards, the reactor was heated (again, at a rate of 4 °C min⁻¹) to either 500 or 600 °C, where gas samples were analyzed in real time every 2 minutes. Finally, the reactor was maintained at the final temperature for 90 minutes before the conclusion of each experiment. A condenser operated at 0 °C was connected to the outlet of the reactor before the Micro GC to serve as a tar and wax trap for certain condensable products, which were further analyzed. A control experiment was performed to assess the degree to which the eutectic hydroxide mixture of Li-KOH could evolve hydrogen absent of any biomass or plastic present (Fig. S10, ESI[†]), revealing minimal H₂ evolution.

Hybrid thermo-electrochemical reactor

Electroreductive cell. Subsequent electrolysis of CO₂ was conducted in a temperature-controlled tubular glass reactor equipped with furnace, gas inlet/outlet, stainless steel caps, and insulated electrode lines depicted in Fig. S5 (ESI[†]). The electrode cables were connected to a computer-controlled BioLogic Model SP-101 potentiostat (Biologic, Seyssinet-Pariset, France). The anode comprised a nickel crucible composed of 99.5%

nickel (nominal volume, 25 mL, Sigma-Aldrich Chemical Co.). The cathode was composed of hot-dip galvanized steel wire (Fi-Shock WC-14200, G90 coating designation according to ASTM A653; zinc coating layer thickness approximately 18 μm). The cathode was fabricated from a 14 Ga wire made into a disk with area of *ca.* 2 cm^2 . Prior to the loading of the blend into the anode crucible, all powdered components were dried at 100 $^\circ\text{C}$ and then thoroughly blended with a mortar and pestle. The anode was capped by a glass-mica ceramic lid and the reactor was assembled and loaded into the furnace. The reactor was heated to 600 $^\circ\text{C}$ at a rate of 10 $^\circ\text{C min}^{-1}$ and then kept at that temperature for 1 h prior to experimentation.

Electrolysis. Electrolysis was performed with an anode (crucible) filled with *ca.* 22 g of a given salt at ambient temperature. The cathode was inserted and the salt was molten at 550 $^\circ\text{C}$ for equilibration. The cell was transferred to the tubular reactor, sealed, and re-equilibrated at a given temperature in the 550–600 $^\circ\text{C}$ range while being purged by nitrogen flow for 40 min. The current density on the cathode during the electrolysis was 120 mA cm^{-2} . Gas flow through the reactor was *ca.* 50 mL min^{-1} . The gas was switched from nitrogen to pure CO_2 ; after 1 h purging of CO_2 , a cyclic voltammetry measurement was then repeated and the electrolysis commenced. A constant current of 240 mA between the cathode and anode was applied for 1 h during electrolysis, while the reactor was maintained at the given temperature. Following electrolysis, the cathode was withdrawn from the reactor at the operational temperature and the reactor was allowed to equilibrate at ambient temperature.

The withdrawn cathode was black, with carbonaceous products of the electrolysis adhering to the cathode surface, a result of the reactions. The nickel anode was observed to be covered by a black coating due to the formation of nickel oxide (Fig. S6, ESI †). The withdrawn cathode was then placed in deionized water and sonicated for 30 min to produce a black suspension (Fig. S6, ESI †). The suspended particles were separated by centrifugation, resuspended with sonication in 1 wt% aqueous HNO_3 solution and dialyzed for 2–7 days at room temperature against excess 1 wt% aqueous HNO_3 solution (membrane MWCO, 12–14 kDa).

Carbon analysis. A UIC Coulometrics (CM150) Carbon Analyzer equipped with a total carbon (TC) furnace module and total inorganic carbon (TIC) acidification module was used to study the distribution of carbon in the various reaction products from both the ATT and electroreductive components, respectively. The inorganic carbon was determined by dissolving the sample in 4N perchloric acid whereas the total carbon was calculated by combustion in pure O_2 at 1000 $^\circ\text{C}$.

Differential scanning calorimetry. During the reactions, condensable waxes and tars were captured in the tar trap and analyzed for any residual plastics *via* Differential Scanning Calorimetry (DSC). A DSC 200 F3 (Netzsch) equipped with Ar purging and liquid nitrogen cooling was utilized for this purpose. The temperature was scanned between 0 and 140 $^\circ\text{C}$ at a rate of 10 $^\circ\text{C min}^{-1}$ for a total of three cooling and heating cycles. Approximately 20 mg of wax was loaded into an

aluminum boat, which was crimped and pierced. The relative crystallinity of the waxes was determined *via* the following equation:

$$X_C (\%) = \frac{\Delta H_M}{\Delta H_M^0} \times 100 \quad (22)$$

where ΔH_M is the melting enthalpy of the wax/tar normalized by weight and ΔH_M^0 is the melting enthalpy of fully crystalline PE with a value of 293 J g^{-1} .⁶⁹

High temperature gel permeation chromatography. The collected waxy products (mostly occurring from the ATT reactions in the presence of LDPE) were additionally analyzed *via* gel permeation chromatography (GPC). This was done to elucidate the relative molecular weight distributions of any polymeric waxy products which were produced and modified during the subsequent SG or ATT reactions. An EcoSEC HT GPC (Tosoh) equipped with a dual flow refractive index (RI) detector and TSKgel Column was used at an operating temperature of 140 $^\circ\text{C}$ with 1,2,4-trichlorobenzene (TCB) as the solvent (wax concentration of 0.1 mg mL^{-1}). The column was purged with TCB while the machine heated up to 140 $^\circ\text{C}$ for 2.5 hours prior to running. The instrument was started when the RI did not deviate from the baseline for greater than 10 minutes. Each sample was run for 70 minutes to ensure all potential polymeric sizes were eluted from the columns. Afterwards, peak identification and integration was performed to yield key parameters such as retention time (min), curve area (mV s), M_n (number average molecular weight), M_w (weight average molecular weight), and M_z (higher average molecular weight). These average molecular weights are expressed broadly by the following equation:

$$M = \frac{\sum N_i M_i^{n+1}}{\sum N_i M_i^n} \quad (23)$$

where $n = 1$ gives $M = M_w$, $n = 2$ gives $M = M_n$, and $n = 3$ gives $M = M_z + 1$. Finally, a ratio of M_w/M_n , also known as the dispersity index, gives an indication of the molecular weight broadness for a certain polymeric sample.⁹² These values were utilized to probe how the thermochemical treatment of the LDPE affects the waxy product slate and potential recovery value.⁹³

Infrared spectroscopy. Fourier transform infrared spectroscopy (FTIR) was used as an additional metric to assess the chemical properties of the solid condensable waxes produced from both the SG and ATT reactions. A Nicolet iS50 FTIR Spectrometer (ThermoFisher Scientific) was used to collect spectra of the wax samples. First, the ambient background was measured and subtracted from the subsequent acquisitions. Each sample was run twice for a total of 64 scans which were then averaged together to produce the spectra. The absorbance was normalized to report the spectra in transmittance (%).^{68,94}

Scanning and transmission electron microscopy. The carbon products from the electrolytic reactions were analyzed with scanning electron microscopy (SEM) and transmission electron microscopy (TEM) to determine the presence of potential CNTs. A 120 kV multipurpose FEI Tecnai (G2 Spirit TWIN) was used

for TEM and a FEI/Philips XL30 FEG ESEM was utilized for the SEM work.

Thermogravimetric analysis. Electrolytic salt compositions were characterized by differential scanning calorimetry (DSC) using a Discovery DSC 250 from TA Instruments. Heating ramp scan rates of 10 °C min⁻¹ were applied. DSC was used in determining the melting curves of the representative eutectic salts used (Fig. S7, ESI†).

Powder X-ray diffraction. XRD patterns were obtained on a 3rd generation Empyrean multipurpose X-ray diffractometer (Malvern PANalytical) equipped with a Cu radiation source and X-ray generator power of 4 kW (max 60 kV, 100 mA) at room temperature. The studied interval was $2\theta = 4\text{--}70^\circ$ with angular resolution of 0.026°.

Author contributions

A.-H. A. P., T. A. H., A. J. M., L. B., and J. M. W. conceived and conceptualized this project. J. M. W. performed the ATT experiments and product categorizations, wrote, and organized most of the paper. M. P. N. and L. B. performed the electroreduction experiments and contributed to the associated Methods and Results details. Z. Q. performed the analysis and data extrapolation for the introductory figures.

Conflicts of interest

There are no conflicts to declare.

Acknowledgements

This work was supported by the Lenfest Center for Sustainability Endowment, Columbia University, New York, NY, 10027, USA. Additional support was provided by the U.S. National Science Foundation AccelNet Program (grant no. 1927336). We thank Guanhe Rim for conducting preliminary experiments at the conception of this project.

References

- M. Gilbert, *Brydson's Plastics Materials: Eighth Edition*, Butterworth-Heinemann, 2016, pp. 2–18.
- C. G. Schirmeister and R. Mülhaupt, *Macromol. Rapid Commun.*, 2022, **43**, 2200247.
- B. C. Gibb, *Nat. Chem.*, 2019, **11**, 394–395.
- M. Eriksen, L. C. M. Lebreton, H. S. Carson, M. Thiel, C. J. Moore, J. C. Borerro, F. Galgani, P. G. Ryan and J. Reisser, *PLoS One*, 2014, **9**, e111913.
- International Energy Agency, *The future of petrochemicals: Towards more sustainable plastics and fertilisers*, 2018, pp. 1–66, DOI: [10.1787/9789264307414-en](https://doi.org/10.1787/9789264307414-en).
- A. Corma, E. Corresa, Y. Mathieu, L. Sauvanud, S. Al-Bogami, M. S. Al-Ghrami and A. Bourane, *Catal. Sci. Technol.*, 2017, **7**, 12–46.
- A. Merrington, *Applied Plastics Engineering Handbook: Processing, Materials, and Applications*, William Andrew Publishing, 2nd edn, 2017, pp. 167–189.
- R. Geyer, J. R. Jambeck and K. L. Law, *Sci. Adv.*, 2017, **3**, 5.
- F. Bauer, T. D. Nielsen, L. J. Nilsson, E. Palm, K. Ericsson, A. Fråne and J. Cullen, *One Earth*, 2022, **5**, 361–376.
- J. R. Jambeck, R. Geyer, C. Wilcox, T. R. Siegler, M. Perryman, A. Andrady, R. Narayan and K. L. Law, *Science*, 2015, **347**, 768–771.
- A. Isobe and S. Iwasaki, *Sci. Total Environ.*, 2022, **825**, 153935.
- L. Lebreton, B. Slat, F. Ferrari, B. Sainte-Rose, J. Aitken, R. Marthouse, S. Hajbane, S. Cunsolo, A. Schwarz, A. Levivier, K. Noble, P. Debeljak, H. Maral, R. Schoeneich-Argent, R. Brambini and J. Reisser, *Sci. Rep.*, 2018, **8**, 1–15.
- M. Edelson, D. Håbesland and R. Traldi, *Mar. Pollut. Bull.*, 2021, **171**, 112720.
- H. Ritchie and M. Roser, Plastic Pollution, <https://ourworldindata.org/plastic-pollution>.
- K. Pabortsava and R. S. Lampitt, *Nat. Commun.*, 2020, **11**, 1–11.
- E. Watt, M. Picard, B. Maldonado, M. A. Abdelwahab, D. F. Mielewski, L. T. Drzal, M. Misra and A. K. Mohanty, *RSC Adv.*, 2021, **11**, 21447–21462.
- Density of plastic, <https://www.statista.com/statistics/595434/plastic-materials-density/>, (accessed 11 March 2021).
- G. Erni-Cassola, V. Zadjelovic, M. I. Gibson and J. A. Christie-Oleza, *J. Hazard. Mater.*, 2019, **369**, 691–698.
- A. C. (Thanos) Bourtsalas, J. Zhang, M. J. Castaldi and N. J. Themelis, *J. Cleaner Prod.*, 2018, **181**, 8–16.
- J. J. Milledge and P. J. Harvey, *J. Chem. Technol. Biotechnol.*, 2016, **91**, 2221–2234.
- A. B. Ross, K. Anastasakis, M. Kubacki and J. M. Jones, *J. Anal. Appl. Pyrolysis*, 2009, **85**, 3–10.
- K. Zhang, W. J. Kim and A. H. A. Park, *Nat. Commun.*, 2020, **11**, 1–9.
- M. A. Alao, O. M. Popoola and T. R. Ayodele, *Clean. Energy Syst.*, 2022, **3**, 100034.
- I. Wender, *Fuel Process. Technol.*, 1996, **48**, 189–297.
- G. Duman, M. A. Uddin and J. Yanik, *Bioresour. Technol.*, 2014, **166**, 24–30.
- O. S. Djandja, Z. Wang, L. Chen, L. Qin, F. Wang, Y. Xu and P. Duan, *Energy Fuels*, 2020, **34**, 11723–11751.
- B. Ciuffi, D. Chiamonti, A. M. Rizzo, M. Frediani and L. Rosi, *Appl. Sci.*, 2020, **10**, 1–35.
- A. Kruse, *Biofuels, Bioprod. Biorefin.*, 2008, **2**, 415–437.
- M. Ni, D. Y. C. Leung, M. K. H. Leung and K. Sumathy, *Fuel Process. Technol.*, 2006, **87**, 461–472.
- J. Dai and K. J. Whitty, *Chem. Eng. Process.*, 2022, **174**, 108902.
- L. Han, Q. Wang, Y. Yang, C. Yu, M. Fang and Z. Luo, *Int. J. Hydrogen Energy*, 2011, **36**, 4820–4829.
- N. Aprianti, M. Faizal, M. Said and S. Nasir, *J. King Saud Univ., Eng. Sci.*, 2022, 1–8.

- 33 A. M. Parvez, S. Hafner, M. Hornberger, M. Schmid and G. Scheffknecht, *Renewable Sustainable Energy Rev.*, 2021, **141**, 110756.
- 34 B. Dou, B. Jiang, Y. Song, C. Zhang, C. Wang, H. Chen, B. Du and Y. Xu, *Fuel*, 2016, **166**, 340–346.
- 35 J. R. Fernandez, J. C. Abanades and G. Grasa, *Chem. Eng. Sci.*, 2012, **84**, 12–20.
- 36 L. À. Barelli, G. Bidini, F. Gallorini and S. Servili, *Energy*, 2008, **33**, 554–570.
- 37 M. R. Stonor, T. E. Ferguson, J. G. Chen and A. H. A. Park, *Energy Environ. Sci.*, 2015, **8**, 1702–1706.
- 38 H. Zhou and A. H. A. Park, *Appl. Energy*, 2020, **264**, 114675.
- 39 M. R. Stonor, N. Ouassil, J. G. Chen and A. H. A. Park, *J. Energy Chem.*, 2017, **26**, 984–1000.
- 40 K. Zhang, N. Ouassil, C. A. O. Campo, G. Rim, W. J. Kim and A. H. A. Park, *J. Ind. Eng. Chem.*, 2020, **85**, 219–225.
- 41 T. E. Ferguson, Y. Park, C. Petit and A. H. A. Park, *Energy Fuels*, 2012, **26**, 4486–4496.
- 42 M. Rahimi, A. Khurram, T. A. Hatton and B. Gallant, *Chem. Soc. Rev.*, 2022, **51**, 8676–8695.
- 43 L. Bromberg, M. P. Nitzsche and T. A. Hatton, *Nanoscale*, 2022, **14**, 13141–13154.
- 44 K. M. Diederichsen, R. Sharifian, J. S. Kang, Y. Liu, S. Kim, B. M. Gallant, D. Vermaas and T. A. Hatton, *Nat. Rev. Methods Primers*, 2022, **2**, 10.
- 45 T. L. Biel-Nielsen, T. A. Hatton, S. N. B. Villadsen, J. S. Jakobsen, J. L. Bonde, A. M. Spormann and P. L. Fosbøl, *ChemSusChem*, 2023, **16**, 7.
- 46 S. Licht, Carbon dioxide to carbon nanotube scale-up, *arXiv*, 2017, preprint, arXiv.1710.07246, DOI: [10.48550/arXiv.1710.07246](https://doi.org/10.48550/arXiv.1710.07246).
- 47 M. Johnson, J. Ren, M. Lefler, G. Licht, J. Vicini, X. Liu and S. Licht, *Mater. Today Energy*, 2017, **5**, 230–236.
- 48 J. Ren, J. Lau, M. Lefler and S. Licht, *J. Phys. Chem. C*, 2015, **119**, 23342–23349.
- 49 Y. Sato and O. Takeda, *Molten Salts Chemistry*, Elsevier, 2013, pp. 451–470.
- 50 O. Al-Juboori, F. Sher, U. Khalid, M. B. K. Niazi and G. Z. Chen, *ACS Sustainable Chem. Eng.*, 2020, **8**, 12877–12890.
- 51 C. Chen, T. Tran, R. Olivares, S. Wright and S. Sun, *J. Sol. Energy Eng.*, 2014, **136**, 7.
- 52 G. J. Janz and M. R. Lorenz, *J. Chem. Eng. Data*, 1961, **6**, 321–323.
- 53 X. Wang, G. Licht, X. Liu and S. Licht, *Sci. Rep.*, 2020, **10**, 1–12.
- 54 S. Licht, M. Lefler, J. Ren and J. Vivini, Electrosynthetic control of CNT conductivity & morphology: Scale-up of the transformation of the greenhouse gas CO₂ into carbon nanotubes by molten carbonate electrolysis, *arXiv*, 2016, preprint, arXiv.1607.02220, DOI: [10.48550/arXiv.1607.02220](https://doi.org/10.48550/arXiv.1607.02220).
- 55 H. V. Ijije, R. C. Lawrence and G. Z. Chen, *RSC Adv.*, 2014, **4**, 35808–35817.
- 56 X. Wang, G. Licht, X. Liu and S. Licht, *Adv. Sustainable Syst.*, 2022, **6**, 2100481.
- 57 X. Liu, G. Licht, X. Wang and S. Licht, *Catalysts*, 2022, **12**, 125.
- 58 M. Keijzer, G. Lindbergh, K. Hemmes, P. J. J. M. van der Put, J. Schoonman and J. H. W. de Wit, *J. Electrochem. Soc.*, 1999, **146**, 2508–2516.
- 59 G. J. Janz and A. Conte, *Electrochim. Acta*, 1964, **9**, 1279–1287.
- 60 S. Li, C. Jiang, J. Liu, H. Tao, X. Meng, P. Connor, J. Hui, S. Wang, J. Ma and J. T. S. Irvine, *J. Power Sources*, 2018, **383**, 10–16.
- 61 W. Weng, L. Tang and W. Xiao, *J. Energy Chem.*, 2019, **28**, 128–143.
- 62 M. Narobe, J. Golob, D. Klinar, V. Francetič and B. Likozar, *Bioresour. Technol.*, 2014, **162**, 21–29.
- 63 H. M. Sheikh, A. Ullah, K. Hong and M. Zaman, *Chem. Eng. Process.*, 2018, **128**, 53–62.
- 64 J. Alvarez, S. Kumagai, C. Wu, T. Yoshioka, J. Bilbao, M. Olazar and P. T. Williams, *Int. J. Hydrogen Energy*, 2014, **39**, 10883–10891.
- 65 G. Guan, M. Kaewpanha, X. Hao and A. Abudula, *Renewable Sustainable Energy Rev.*, 2016, **58**, 450–461.
- 66 S. Liu, P. A. Kots, B. C. Vance, A. Danielson and D. G. Vlachos, *Sci. Adv.*, 2021, **7**, 1–9.
- 67 M. R. Stonor, J. G. Chen and A. H. A. Park, *Int. J. Hydrogen Energy*, 2017, **42**, 25903–25913.
- 68 J. V. Gulmine, P. R. Janissek, H. M. Heise and L. Akcelrud, *Polym. Test.*, 2002, **21**, 557–563.
- 69 Crystallinity/Degree of Crystallinity, <https://www.netzsch-thermal-analysis.com/en/contract-testing/glossary/crystallinity-degree-of-crystallinity/>, (accessed 11 March 2021).
- 70 X. Ye and T. Sridhar, *Macromolecules*, 2005, **38**, 3442–3449.
- 71 R. Wartena, J. Winnick and P. H. Pfromm, *J. Appl. Electrochem.*, 2002, **32**, 415–424.
- 72 M. Chase, *JANAF Thermochemical Tables*, American Chemical Society and American Institute for Physics of the National Bureau of Standards, 3rd edn, 1986.
- 73 Y. Izaki, Y. Mugikura, T. Watanabe, M. Kawase and J. R. Selman, *J. Power Sources*, 1998, **75**, 236–243.
- 74 M. D. Ingram and G. J. Janz, *Electrochim. Acta*, 1965, **10**, 783–792.
- 75 M. S. Yazici and J. R. Selman, *J. Electroanal. Chem.*, 1998, **457**, 89–97.
- 76 J. P. T. Vossen, L. Plomp and J. H. W. de Wit, *J. Electrochem. Soc.*, 1994, **141**, 3040–3049.
- 77 L. Qingfeng, F. Borup, I. Petrushina and N. J. Bjerrum, *J. Electrochem. Soc.*, 1999, **146**, 2449–2454.
- 78 H. Yin, X. Mao, D. Tang, W. Xiao, L. Xing, H. Zhu, D. Wang and D. R. Sadoway, *Energy Environ. Sci.*, 2013, **6**, 1538–1545.
- 79 H. V. Ijije, R. C. Lawrence, N. J. Siambun, S. M. Jeong, D. A. Jewell, D. Hu and G. Z. Chen, *Faraday Discuss.*, 2014, **172**, 105–116.
- 80 W. H. Kruesi and D. J. Fray, *J. Appl. Electrochem.*, 1994, **24**, 1102–1108.
- 81 R. D. Weaver, *ECS Proc. Vol.*, 1981, **1981–1989**, 316–333.
- 82 C. Cui, S. Li, J. Gong, K. Wei, X. Hou, C. Jiang, Y. Yao and J. Ma, *Mater. Renew. Sustain. Energy*, 2021, **10**, 1–24.
- 83 X. Wang, X. Liu, G. Licht and S. Licht, *Sci. Rep.*, 2020, **10**, 1–7.
- 84 B. Deng, J. Tang, X. Mao, Y. Song, H. Zhu, W. Xiao and D. Wang, *Environ. Sci. Technol.*, 2016, **50**, 10588–10595.

- 85 W. Cai, R. Chen, Y. Yang, M. Yi and L. Xiang, *Crystals*, 2018, **8**, 1–8.
- 86 H. Effenberger, *Z. Kristallogr.*, 1979, **150**, 133–138.
- 87 P. Rajasekaran, H. Kannan, S. Das, M. Young and S. Santra, *AIMS Environ. Sci.*, 2016, **3**, 439–455.
- 88 S. Rakshit, S. Ghosh, S. Chall, S. S. Mati, S. P. Moulik and S. C. Bhattacharya, *RSC Adv.*, 2013, **3**, 19348–19356.
- 89 V. D. Jović, V. Maksimović, M. G. Pavlović and K. I. Popov, *J. Solid State Electrochem.*, 2006, **10**, 373–379.
- 90 J. Ren and S. Licht, *Sci. Rep.*, 2016, **6**, 1–11.
- 91 A. van Giezen and B. Wiegman, *Transp. Res. Interdiscip. Perspect.*, 2020, **5**, 100115.
- 92 S. G. Hatzikiriakos, *Polym. Eng. Sci.*, 2000, **40**, 2279–2287.
- 93 M. Arabiourrutia, G. Elordi, G. Lopez, E. Borsella, J. Bilbao and M. Olazar, *J. Anal. Appl. Pyrolysis*, 2012, **94**, 230–237.
- 94 T. G. Feric, S. T. Hamilton, N. M. Cantillo, A. E. Imel, T. A. Zawodzinski and A. H. A. Park, *J. Phys. Chem. B*, 2021, **125**, 9223–9234.